Ab initio calculations of interaction energies of magnetic layers in noble metals: Co/Cu(100)

P. Lang, L. Nordström,* K. Wildberger, R. Zeller, and P. H. Dederichs
Institut für Festkörperforschung, Forschungszentrum Jülich, D-52425 Jülich, Germany

T. Hoshino
College of Engineering, Shizuoka University, Hamatsu 432, Japan
(Received 20 January 1995; revised manuscript received 22 August 1995)

We present *ab initio* calculations for the interlayer exchange coupling of magnetic Co(100) layers in Cu. The calculations are based on a Korringa-Kohn-Rostoker Green's function method for planar defects and apply the frozen potential approximation, allowing a direct calculation of the interaction via single-particle energies. Thus the subtraction of large total energies is avoided and efficient calculations for large layer thicknesses are enabled. By dividing the two-dimensional Brillouin zone into areas around different stationary points $\mathbf{q}_i$, an analysis of the asymptotic behavior is given. The different dependences of the short and long oscillation periods on the thickness of the magnetic layers are explained by the $\mathbf{q}_\parallel$- and symmetry-projected density of states of the Co layers. The effects of roughness on the interlayer coupling are simulated, leading to a strong reduction of the amplitudes and a suppression of the short-wavelength period. Our calculations are in good agreement with experiments and give a consistent picture of interlayer coupling in Co/Cu(100), as far as both the dependence on the thickness of the magnetic layers as well as the dependence on roughness are concerned.

I. INTRODUCTION

Long-ranged magnetic coupling of magnetic layers was first observed for Fe/Cr/Fe by Grünberg *et al.*,[1] who detected an antiferromagnetic coupling of the iron layers. Subsequently the coupling has been found to be of oscillatory nature with varying nonmagnetic spacer thickness and has been observed for a large variety of systems.[2] This so-called interlayer exchange coupling (IXC) has attracted a lot of attention, mainly because of the close connection to the technologically important giant magnetoresistance (GMR) effect.

Today there is strong evidence that the observed oscillation periods are in accordance with a RKKY picture.[3] The RKKY model predicts the different oscillation periods to stem from extremal spanning vectors, so-called calipers, of the Fermi surface of the spacer material.[3,4] However, the existence of these oscillation periods does not rely on some of the strong restrictions entering the original RKKY model, like, e.g., the pointlike *s*-*d* exchange potential of the magnetic layer. Nevertheless, in the following we will adopt the usual convention and refer to these oscillations as RKKY oscillations.

Since the first experimental observations, the quality of the experiments has improved continuously. A popular technique to observe the magnetic coupling is the magneto-optical Kerr effect (MOKE) applied to samples grown in a wedge geometry. This sample geometry makes it possible to study at one and the same sample the coupling as a continuously varying function of the spacer thickness.

Although successful, RKKY-like models have clear limitations in that they can neither give the amplitudes nor the phases of the oscillations and that they are only valid asymptotically at large interlayer distances. In order to make more quantitative predictions *ab initio* calculations for realistic systems must be performed.

Several different first-principles calculations have been reported which have observed oscillatory behavior.[5–8] These calculations may be divided into two main categories. The first category is concerned with calculations on supercells,[5,6] i.e., for a periodic array of magnetic layers, and should therefore be comparable to experiments performed on multilayers. The second one considers the interaction of two layers (bilayers) and corresponds more closely to the experiments on wedge samples.[7,8]

It is the purpose of this paper to show that the exchange coupling of bilayers can be calculated accurately up to rather large distances within a first-principles approach, and that the resulting energies are in good agreement with experiments. The range of thicknesses in the calculations is so large that it also allows one to discuss the asymptotic RKKY behavior and its relation to the Fermi surface. Using the same method we have already presented first results for Fe and Co monolayers[7] and for thicker Co layers in fcc Cu.[9] In these calculations we found oscillation periods in agreement with those predicted by the RKKY model. Here, we give a more detailed account of this work, stressing the asymptotic behavior and in particular the dependence of the oscillations on the magnetic layer thickness which can strongly modify the amplitude of the different oscillation periods. Moreover, we explain in detail our method used for the calculation of the IXC energies.

First, the calculational method for the interlayer exchange coupling (ILXC), which was already used in previous papers[7,9] will be derived in Sec. II In Sec. III we will present results for magnetic Co layers in the noble metal Cu for the orientation (100) and discuss their relation to the Fermi surface of Cu and the electronic structure of the Co layers. In addition to these calculations on perfectly ordered layers, we give a transparent discussion of the effect of steplike interface roughness and show that roughness can strongly modify the interaction. A detailed comparison with experiments concludes this section.

II. THEORETICAL METHOD

The system we aim to study consists of two parallel magnetic layers embedded in a nonmagnetic host and separated by a variable number of atomic host layers (here up to 32). The magnetic layer consists of several atomic layers (here up to 11). The electronic structure for this system is calculated using density functional theory and the Korringa-Kohn-Rostoker (KKR) Green's function method.[12]

For calculations within the local spin density approximation (LSDA) of density functional theory the task is generally to solve the effective one-electron Schrödinger equation given by a Hamiltonian

$$H=-\nabla^2+V^{\sigma}(\mathbf{r}). \tag{1}$$

The spin-dependent potential $V^{\sigma}(\mathbf{r})$ is a functional of the charge $\rho(\mathbf{r})$ and magnetization $m(\mathbf{r})$ densities, which in turn are obtained from the occupied eigenfunctions. In the Green's function method the calculation of the eigenfunctions is avoided. Rather one aims at directly calculating the Green's function $G=(\varepsilon-H)^{-1}$ of the system. As will be discussed below, one views the difference of the potentials from a known reference case as a perturbation. This leads to a Dyson equation for the Green's functions. The densities are obtained from the imaginary part of this perturbed Green's function by integrating over all occupied energies. Whatever procedure is used, Eq. (1) must always be solved self-consistently by iteration.

We will now first review the KKR Green's function method,[13] in particular its extension to layered systems.[12] First, we treat a single perturbing layer and then the case of two interacting layers. Especially the so-called Lloyd's formula[14] for the change of the integrated density of states will be discussed. The expression for the interlayer interaction is subsequently derived[7,9] by means of this formula. Although this expression is only based on a calculation of single-particle energies, we demonstrate its accuracy in calculations for the exchange coupling of magnetic impurities. Finally in this section the role of finite temperatures adopted in this method is discussed. In the following most quantities should carry in general a spin index $\sigma=\pm$, which for convenience will be skipped when not absolutely necessary.

A. KKR Green's function method

The basic concept within the KKR Green's function method[13,12] is that for a crystal lattice potential $V(\mathbf{r})=\Sigma_n V_n(\mathbf{r})$ the Green's function corresponding to Hamiltonian (1) can be written as

$$G(\mathbf{r}_n,\mathbf{r}'_{n'};\varepsilon)=G^s_n(\mathbf{r},\mathbf{r}';\varepsilon)\,\delta_{n,n'} + \sum_{LL'} R_{nL}(\mathbf{r};\varepsilon)G_{nL,n'L'}(\varepsilon)R_{n'L'}(\mathbf{r}';\varepsilon), \tag{2}$$

where the matrix elements $G_{nL,n'L'}$, the so-called structural Green's function (SGF), describe the multiple scattering, while G^s_n is the single-scattering Green's function depending only on the potential within the cell n. Here we have used cell-centered coordinates $\mathbf{r}_n=\mathbf{R}_n+\mathbf{r}$, where $\mathbf{R}_n$ is a lattice vector and $\mathbf{r}$ is only defined within the Wigner-Seitz cell of this lattice point. The SGF is a matrix over combined indices labeled by the atomic positions n and the angular momenta $L=\{\ell,m\}$ expanded around n. In the present paper we will restrict ourselves to the atomic sphere approximation (ASA) for the potential. In this approximation we assume spherically symmetric potentials in each Wigner-Seitz sphere, which slightly overlap, i.e., $V_n(\mathbf{r})=V_n(r)$. Then $R_{nL}(\mathbf{r};\varepsilon)=R_{n\ell}(r;\varepsilon)Y_L(\hat{r})$, where $R_{n\ell}(r;\varepsilon)$ is the regular solution of the following radial equation within the cell n:

$$\left(-\frac{d^2}{dr^2}+\frac{\ell(\ell+1)}{r^2}+V_n(r)-\varepsilon\right)rR_{n\ell}(r;\varepsilon)=0. \tag{3}$$

The single-scattering Green's function is given in terms of the regular, R_{nL}, and the irregular, H_{nL}, solutions within the sphere,

$$G^s_n(\mathbf{r},\mathbf{r}';\varepsilon)=\sqrt{\varepsilon}\sum_L R_{nL}(\mathbf{r}_<;\varepsilon)H_{nL}(\mathbf{r}_>;\varepsilon), \tag{4}$$

where $\mathbf{r}_<$ is the one of $\mathbf{r}$ and $\mathbf{r}'$ which is closest to the origin and $\mathbf{r}_>$ is the complement. By constructing the full Green's function one is always able to calculate the charge and magnetization densities $\rho(\mathbf{r})$ and $m(\mathbf{r})$ through the imaginary part,

$$\rho(\mathbf{r})=-\frac{1}{\pi}\int_{-\infty}^{\infty} f(\varepsilon)\,\mathrm{Im}[G^+(\mathbf{r},\mathbf{r};\varepsilon)+G^-(\mathbf{r},\mathbf{r};\varepsilon)]\,d\varepsilon, \tag{5a}$$

$$m(\mathbf{r})=-\frac{1}{\pi}\int_{-\infty}^{\infty} f(\varepsilon)\,\mathrm{Im}[G^+(\mathbf{r},\mathbf{r};\varepsilon)-G^-(\mathbf{r},\mathbf{r};\varepsilon)]\,d\varepsilon. \tag{5b}$$

These integrals extend over all occupied states, with the occupation described by the Fermi-Dirac distribution $f(\varepsilon)$. The reason for introducing a finite temperature into the calculation will be discussed below in Sec. II F.

Starting with a known structural Green's function G^0 as reference one can get the SGF for a system with different potentials, but with the same underlying lattice, via a Dyson equation

$$G(\varepsilon)=G^0(\varepsilon)+G^0(\varepsilon)\Delta t(\varepsilon)G(\varepsilon). \tag{6}$$

For finite matrices this equation can be solved by matrix inversion. Here $\Delta t(\varepsilon)$ is the difference between the t matrices of the real system, $t(\varepsilon)$, and the reference system, $t^0(\varepsilon)$. It is diagonal in the $\{nL\}$ indices and is given by

$$\Delta t_{nL,n'L'}(\varepsilon)=\delta_{nL,n'L'}\{t_{n,L}(\varepsilon)-t^0_{n,L}(\varepsilon)\} =\delta_{nL,n'L'}\int_0^{S_n} r^2 j_{\ell}(r\sqrt{\varepsilon})\{V_n(r)R_{n\ell}(r;\varepsilon) - V^0_n(r)R^0_{n\ell}(r;\varepsilon)\}dr, \tag{7}$$

where S_n is the radius of the atomic sphere and $j_{\ell}(r\sqrt{\varepsilon})$ is a spherical Bessel function. This procedure of introducing reference states will be repeatedly used in the following. For instance, as will be discussed below, the SGF of the host will be considered as the perturbed SGF in the first step and as

the reference SGF in the next one. In the following we will consistently denote quantities belonging to the proper reference state with a 0 as superscript.

If the change of the potential is localized to a certain region in space, the Dyson equation can be solved in real space by matrix inversion, since Δt vanishes outside this perturbed region. This method has been used extensively for studying, e.g., magnetic impurities in metals.[13,15] On the other hand, if the perturbed potential has some sort of translational invariance, Eq. (6) has to be solved in reciprocal space, i.e., by Fourier transformation. For instance, to obtain the SGF for the noble metal crystal, which represents the first step in our method, we consider as a reference system free electrons ($V^0=0$) within a fcc lattice for which the SGF is known analytically. Now making use of the translational invariance, the Dyson equation (6) is solved separately for each $\mathbf{k}$ point in the three-dimensional (3D) Brillouin zone (BZ),

$$G(\mathbf{k};\varepsilon)=G^0(\mathbf{k};\varepsilon)+G^0(\mathbf{k};\varepsilon)t(\varepsilon)G(\mathbf{k};\varepsilon). \tag{8}$$

Here the matrices have only angular momentum indices L,L'. The real-space SGF is then obtained via a Fourier transform,

$$G_{nL,n'L'}(\varepsilon)=\Omega_{\mathrm{BZ}}^{-1}\int_{\mathrm{BZ}} G_{L,L'}(\mathbf{k};\varepsilon)\exp\{i\mathbf{k}\cdot(\mathbf{R}_n-\mathbf{R}_{n'})\}d\mathbf{k}, \tag{9}$$

where Ω_{BZ} is the volume of the 2D BZ and $\mathbf{R}_n$ is a lattice vector.

B. One magnetic layer

As the second step we consider a crystal being perturbed by one layer (which, however, may consist of several atomic layers). The three-dimensional translational invariance is then broken and only the two-dimensional periodicity in the layer plane remains. This means that the symmetry label is reduced from $\mathbf{k}=\mathbf{k}_\parallel+\mathbf{k}_\perp$ to $\mathbf{k}_\parallel$, and the appropriate reference SGF will have a mixed real and reciprocal space representation. Hence we have to transform the SGF of the ideal crystal which now serves as the reference SGF into this representation by integrating over $\mathbf{k}_\perp$,

$$G^0_{iL,i'L'}(\mathbf{k}_\parallel;\varepsilon)=\frac{d}{2\pi}\int_{-\pi/d}^{\pi/d} G^0_{L,L'}(\mathbf{k};\varepsilon) \times\exp\{i\mathbf{k}\cdot(\mathbf{R}_i-\mathbf{R}_{i'})\}d\mathbf{k}_\perp . \tag{10}$$

Here the i index denotes the atomic layers within the crystal and d the distance between adjacent monolayers. The division of $\mathbf{k}$ into $\mathbf{k}_\parallel$ and $\mathbf{k}_\perp$ depends of course on the orientation of the layers. For the orientation [100] the 2D BZ for $\mathbf{k}_\parallel$ has the form of a square as shown in Fig. 1, and by definition $\mathbf{k}_\perp$ is normal to the plane of this 2D BZ.

The SGF for the perturbed system is now obtained from the Dyson equation

$$G(\mathbf{k}_\parallel;\varepsilon)=G^0(\mathbf{k}_\parallel;\varepsilon)+G^0(\mathbf{k}_\parallel;\varepsilon)\Delta t(\varepsilon)G(\mathbf{k}_\parallel;\varepsilon), \tag{11}$$

where the matrices have $\{iL\}$ indices. By Fourier transforming back into real space and adding the single-scattering Green's function the total Green's function can be calculated

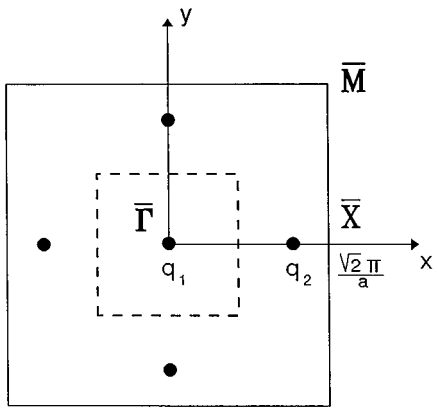

FIG. 1. Two-dimensional Brillouin zone for the [100] orientation. Shown also are the positions of the five stationary points, the two inequivalent ones of which are located at $\mathbf{q}_1=0=\bar{\Gamma}$ and $\mathbf{q}_2=(1.08,0)\pi/a$. The dashed line indicates the subdivision of the 2D BZ into areas A_i $(i=1,2)$ around the stationary points (Sec. II E).

and hence the densities through Eq. (2). These densities are used to calculate a new potential $V(\mathbf{r})$, which gives a new Δt through Eq. (5) and which then enters into Eq. (11). This procedure is iterated until self-consistency is reached.

Besides the charge and magnetization densities also the density of states (DOS) may be obtained directly from the imaginary part of the Green's function,

$$n(\varepsilon)=-\frac{1}{\pi}\int \mathrm{Im}G(\mathbf{r},\mathbf{r};\varepsilon)d\mathbf{r}. \tag{12}$$

However, generally in multiple-scattering methods the difference in the energy integrated DOS (IDOS) due to the perturbation, $\Delta N(\varepsilon)$, can be expressed as a Lloyd's formula.[14] In the following we will use the form suggested by Drittler *et al.*[16] properly generalized to the case of 2D translation symmetry,

$$\Delta N(\mathbf{k}_\parallel;\varepsilon)=\frac{1}{\pi}[\mathrm{Im}\ \ln\det\{\alpha_0(\varepsilon)\alpha^{-1}(\varepsilon)\} -\mathrm{Im}\ \ln\det\{1-G^0(\mathbf{k}_\parallel;\varepsilon)\Delta t(\varepsilon)\}]. \tag{13}$$

The α_0 and α matrices in the first term describe the single-site scattering at the unperturbed and perturbed potentials, respectively, as has been described in detail in Ref. 16. As we will see later this term is of no importance for the interaction. Instead one should concentrate on the second term where the unperturbed SGF matrix and the self-consistently calculated Δt matrix of the perturbation occur. This term takes care of all multiple scattering within the perturbed region. The determinants in Eq. (13) have only to be taken over the perturbed layer, i.e., where Δt differs from zero. Since the imaginary part of the logarithm of a complex quantity is the same as the argument of this complex quantity, the right-hand side of Eq. (13) represents a phase factor. That the IDOS is connected to a phase factor is well known for impurities. This is expressed by Friedel's sum rule, which is in fact just a special case of Lloyd's formula.

C. Two magnetic layers

When finally two layers, separated by an essentially unperturbed spacer layer in between, are considered we can still use the same technique as for one layer, treating the two layers and the intermediate region as a single perturbed entity. However, if the two layers are well separated, such a calculation would require an immense computing effort, due to the size of the matrices entering the Dyson equation. Additionally several separate calculations have to be performed for all the different spacer thicknesses in between the layers. For each calculation a very good convergence in the densities is necessary in order to obtain the needed accuracy of the total energy.

Instead we calculate in the present paper only the single-layer case self-consistently. The further change in the electronic structure when the two individual layers are allowed to interact is then calculated within the frozen potential approximation (FPA),[17] which is also known as the ''force theorem.'' In this approximation the potentials of each one of the magnetic layers or the spacer layer in between are supposed not to change in any significant way by the presence of the other layer. However, the corresponding change in charge and magnetization densities is implicitly taken into account in the calculation of the interaction energies, although in a non-self-consistent way. This is expected to be a sound approximation when calculating IXC energies for spacers like Cu where, in contrast to transition metals like Cr or Pd, enhancement effects of the magnetization density are very small.[18] Additionally, the magnetic moments are well saturated for Co layers in Cu, so that the Co potential is insensitive to small changes in the environment and nothing dramatic would occur in an iteration procedure. Care should, however, be taken when this approximation is applied to other systems.

The adoption of the frozen potential approximation has two major numerical advantages, besides the gain in computing efforts. First, as will be discussed later on, the total energies are easily calculated with the help of the so-called force theorem.[17] Second, as now will be shown, a manipulation of Lloyd's formula (13) gives a direct expression for the change in the IDOS solely due to the interaction of the two layers, thus avoiding the problem of the numerical subtraction of large energies. Moreover, it allows a transparent discussion of the asymptotic behavior, as demonstrated in Sec. III.

D. Interacting IDOS

The change of the IDOS due to the interaction of the two layers 1 and 2 is given by

$$\Delta N_{\rm int}(\mathbf{k}_\parallel;\varepsilon)=\Delta N_{1+2}(\mathbf{k}_\parallel;\varepsilon)-\Delta N_1(\mathbf{k}_\parallel;\varepsilon)-\Delta N_2(\mathbf{k}_\parallel;\varepsilon), \tag{14}$$

where ΔN_{1+2} refers to the change of the IDOS with respect to the host crystal as a reference when both layers are embedded in the crystal, and where ΔN_1 and ΔN_2 give the corresponding changes for the single layers 1 and 2, respectively. The subtraction of these contributions guarantees that $\Delta N_{\rm int}$ only refers to the changes arising from the interaction of the two layers. Since Eq. (13) for $\Delta N(\varepsilon)$ is valid for an arbitrary perturbation Δt, we can apply this equation both to the case of two layers, by setting $\Delta t=\Delta t_1+\Delta t_1$, as well as to the single-layer cases, setting $\Delta t=\Delta t_1$ or $\Delta t=\Delta t_2$. Due to the frozen potential approximation, the t matrices Δt_1 and Δt_2 are the ones self-consistently determined for the single layers and as such are not changed by the interaction. Since the same is also true for the α matrices in Eq. (13), these single-site contributions cancel directly when inserting into Eq. (14), so that $\Delta N_{\rm int}$ is only determined by the multiple-scattering parts,

$$\Delta N_{\rm int}(\mathbf{k}_\parallel;\varepsilon)=-\frac{1}{\pi}{\rm Im}[\ln\det\{1-G^0(\Delta t_1+\Delta t_2)\}-\ln\det\{1-G^0\Delta t_1\}-\ln\det\{1-G^0\Delta t_2\}]. \tag{15}$$

Using some standard algebraic identities—i.e., the sum of logarithms is the logarithm of the product—$\det(A)\det(B)=\det(AB)$ and $\{\det(A)\}^{-1}=\det(A^{-1})$, we arrive at the expression

$$\Delta N_{\rm int}(\mathbf{k}_\parallel;\varepsilon)=-\frac{1}{\pi}{\rm Im}\ln\det\{M(\mathbf{k}_\parallel;\varepsilon)\}, \tag{16}$$

where the matrix M, describing only the interaction effects, is given by

$$M(\mathbf{k}_\parallel;\varepsilon)=(1-G^0\Delta t_1)^{-1}\{1-G^0(\Delta t_1+\Delta t_2)\}\times(1-G^0\Delta t_2)^{-1}. \tag{17}$$

Now, the expression within the curly brackets can be written as

$$1-G^0(\Delta t_1+\Delta t_2)=(1-G^0\Delta t_1)(1-G^0\Delta t_2)-G^0\Delta t_1G^0\Delta t_2, \tag{18}$$

so that $M(\mathbf{k}_\parallel;\varepsilon)$ is given by

$$M(\mathbf{k}_\parallel;\varepsilon)=1-(1-G^0\Delta t_1)^{-1}G^0\Delta t_1G^0\Delta t_2(1-G^0\Delta t_2)^{-1}. \tag{19}$$

Since $G^0\Delta t_1$ commutes with $(1-G^0\Delta t_1)^{-1}$, the final result is

$$M(\mathbf{k}_\parallel;\varepsilon)=1-G^0\tau_1G^0\tau_2 \tag{20}$$

and correspondingly

$$\Delta N_{\rm int}(\mathbf{k}_\parallel;\varepsilon)=-\frac{1}{\pi}{\rm Im}\ln\det(1-G^0\tau_1G^0\tau_2). \tag{21}$$

Here the τ matrix

$$\tau_i(\mathbf{k}_\parallel;\varepsilon)=\Delta t_i(\varepsilon)\{1-G^0(\mathbf{k}_\parallel;\varepsilon)\Delta t_i(\varepsilon)\}^{-1}(\text{for } i=1,2) \tag{22}$$

describes all the scattering processes within the single layer i and depends, contrary to the atomic t matrix $\Delta t_i(\varepsilon)$, in addition to the energy ε also on $\mathbf{k}_\parallel$.

Equation (21) represents the central result of this section. The determinant is of the order $mL_{\rm max}$, where m is the number of atomic layers within one magnetic layer. Thus the

numerical effort involved in evaluating $\Delta N_{\rm int}$ is independent of the number of atomic spacer layers n separating the two layers.

The SGF's which explicitly enter Eq. (21) connect the two layers, while the ones entering τ_i in Eq. (22) are localized within each layer. Therefore Eq. (21) can be viewed as arising due to the interference of Bloch electrons scattering between the two layers. The propagation of the electrons through the spacer layer is described by the nonlocal SGF G^0 while the scattering at each layer is described by the t matrix τ of this layer. Note that these two quantities are calculated self-consistently from first principles. The layer SGF $G^0(\mathbf{k}_\parallel;\varepsilon)$ is calculated from the crystal SGF through Eq. (10) and $\Delta t(\varepsilon)$ is calculated from the self-consistent potential of the layer through Eq. (7). Further it is clear that if, as in the present paper, one considers two magnetic layers in a nonmagnetic metal, all spin dependence enters through the spin-dependent potential of the magnetic layer, i.e., through Δt or τ.

In the case of relatively weak scattering the logarithm in Eq. (21) can be expanded in a power series. Since $\ln\det(A)=\mathrm{Tr}\ln(A)$, we can write

$$\begin{aligned}\Delta N_{\rm int}(\mathbf{k}_\parallel;\varepsilon) &= -\frac{1}{\pi}\mathrm{Im\ Tr}\ln(1-G^0\tau_1G^0\tau_2)\\ &= \frac{1}{\pi}\mathrm{Im\ Tr}\sum_{n=1}^{\infty}\frac{1}{n}(G^0\tau_1G^0\tau_2)^n \quad (\text{for } \|G^0\tau_1G^0\tau_2\|<1)\\ &\approx \frac{1}{\pi}\mathrm{Im\ Tr}G^0\tau_1G^0\tau_2 \quad (\text{when } \|G^0\tau_1G^0\tau_2\|\ll 1),\end{aligned} \tag{23}$$

where the double vertical lines indicate a matrix norm.

E. Interaction energy

To study the interaction energy we will work with the grand canonical function Ω to take the advantage of using finite temperatures in the numerical calculation (see below). Formally the density functional theory has been generalized to finite temperatures by Mermin.[19] In principle we follow that work, but since the temperature effect on the LSDA potential is very small for the temperatures used in this study, we ignore this contribution. So in principle the temperature is only introduced in the single-particle spectrum. When calculating the grand canonical function it is natural to divide it into a single-particle part Ω_s and a double-counting part $\Omega_{\rm DC}$, $\Omega_{\rm tot}=\Omega_s+\Omega_{\rm DC}$. The single-particle contribution is usually written as an integral over the DOS $n(\varepsilon)$,

$$\Omega_s=-kT\int_{-\infty}^{\infty}\ln[1+\exp\{(\mu-\varepsilon)/kT\}]n(\varepsilon)d\varepsilon, \tag{24}$$

where μ is the chemical potential, k Boltzmann's constant, and T the temperature. By a partial integration this can be rewritten as an integral over the IDOS $N(\varepsilon)$,

$$\Omega_s=-\int_{-\infty}^{\infty}f(\varepsilon)N(\varepsilon)d\varepsilon. \tag{25}$$

This formula differs from Eq. (3) in Ref. 7 which we used in previous calculations. At finite temperatures the grand canonical function Ω_s has the desired extremal properties for accurate total-energy calculations[20] and is also numerically more easily evaluated than the single-particle energies alone [Eq. (3) in Ref. 7]. Now we want to calculate the interaction energy $\Delta\Omega$ of the two magnetic layers. The single-particle contribution $\Delta\Omega_s$ is obtained by directly inserting the corresponding IDOS, properly integrated over the 2D BZ and summed over the spin directions. Thus

$$\Delta\Omega_s=\frac{-1}{A_{\rm BZ}}\int_{-\infty}^{\infty}d\varepsilon f(\varepsilon)\int_{\rm BZ}d\mathbf{k}_\parallel\sum_\sigma\Delta N_{\rm int}^\sigma(\mathbf{k}_\parallel,\varepsilon), \tag{26}$$

where $A_{\rm BZ}$ is the area of the 2D BZ. An additional contribution from the double-counting energies $\Omega_{\rm DC}$ would arise, which is neglected in the frozen potential approximation (FPA). The validity of this approximation for the exchange is discussed in the next subsection. The interlayer exchange energy $E_{\rm IXC}$ is defined as the difference in $\Delta\Omega$ between the ferromagnetic and antiferromagnetic configuration of the two layers, $E_{\rm IXC}=\Delta\Omega_{\rm F}-\Delta\Omega_{\rm AF}$. Thus in FPA we only need to evaluate the interacting IDOS $\Delta N_{\rm int}^{\rm F}$ and $\Delta N_{\rm int}^{\rm AF}$ for the two configurations. The final expression for the interlayer exchange coupling is

$$E_{\rm IXC}=\frac{1}{\pi A_{\rm BZ}}\int_{-\infty}^{\infty}d\varepsilon f(\varepsilon)\int_{\rm BZ}d\mathbf{k}_\parallel\mathrm{Im}\ln\frac{\det(1-G^0\tau_1^+G^0\tau_2^+)\det(1-G^0\tau_1^-G^0\tau_2^-)}{\det(1-G^0\tau_1^+G^0\tau_2^-)\det(1-G^0\tau_1^-G^0\tau_2^+)}. \tag{27}$$

Here the spin indices + and − denote the local majority and minority states, respectively. Since the two layers are of the same type, the spin-dependent τ matrices of the isolated layers entering Eq. (27) are actually equal. The numerator refers to the ferromagnetic configuration and the denominator to the antiferromagnetic one. In the case of weak scattering this expression for the IXC energy can be approximated in the same way as in Eq. (23). So in this limit the exchange energy becomes

$$E_{\mathrm{IXC}} \cong \frac{-1}{\pi A_{\mathrm{BZ}}} \int_{-\infty}^{\infty} d\varepsilon f(\varepsilon) \int_{\mathrm{BZ}} d\mathbf{k}_{\parallel} \mathrm{Im}\mathrm{Tr} G^0 \Delta\tau_1 G^0 \Delta\tau_2 , \tag{28}$$

where $\Delta\tau_i = \tau_i^+ - \tau_i^-$ is the exchange splitting of the τ matrix of layer i. This limit is essentially the RKKY picture: The spin-asymmetry potential of layer 1 induces a magnetization at layer 2, through $G^0 \Delta\tau_1 G^0$, which interacts with the local spin-asymmetry potential $\Delta\tau_2$.

It can be shown that the integrand in Eq. (27) oscillates rapidly in both variables ε and $\mathbf{k}_{\parallel}$ for large interlayer distances. This leads to huge cancellations within the integrals. With a stationary-phase approximation it has been shown[3] that asymptotically for large distances there will only be contributions to the integrals arising from the Fermi energy ε_F, respectively, from special points in the 2D BZ where the integrand is stationary, so-called stationary points (Fig. 1). These points correspond to the Fermi surface calipers[3,4] of the RKKY theory.

F. Single-particle energies versus total energies

Here we want to demonstrate that within the frozen potential approximation the single-particle energies alone allow a reliable calculation of the interlayer exchange coupling, so that the double-counting contributions can be neglected. Thus no new self-consistent calculations for the system of two interacting magnetic layers are necessary. This does not only lead to a large saving of computer time, but also allows a very transparent discussion of the asymptotic behavior of the IXC as presented in Sec. III B.

Since for larger distances the interaction energies are very small, the frozen potentials of the single layers represent very good trial potentials to calculate the interaction in a variational approach. However, unfortunately the double-counting terms cannot be neglected in general. For instance, Gautier *et al.*[21] have shown that for the case of interacting impurities the double-counting contributions are significant and that, e.g., the single-particle contribution alone does not reproduce the correct result in the limit of weak potentials. Then the interaction of the screened potential of one impurity with the bare potential of the other one determines the interaction energies, while in the single-particle energies both potentials are screened. On the other hand, Oswald *et al.*[18] have shown that due to the extremal properties of the double-counting terms the *exchange interaction* of two magnetic impurities is well given by the single-particle energies alone, provided that the polarization and exchange enhancement of the host are sufficiently small, which should be well satisfied for the noble metals. The same arguments can be applied for the exchange interaction of two magnetic layers.

TABLE I. Exchange interaction $E_{\mathrm{F}} - E_{\mathrm{AF}}$ (in meV) for two Co impurities in Cu as a function of the separation. The values FPA1 and FPA2 refer to two different frozen potential approximations and are compared with total-energy results from fully self-consistent calculations (see text).

	FPA1	FPA2	Full scf
First neighbor (110)	−92.6	−72.3	−77.1
Second neighbor (200)	9.8	15.5	15.1
Third neighbor (211)	−2.4	−4.2	−4.5
Fourth neighbor (220)	3.7	6.1	6.7
Eighth neighbor (400)	−1.6	−2.4	−2.7

In the following we pursue the statement of Oswald *et al.*[18] in numerical calculations for the exchange interaction of two Co impurities in Cu. Table I shows the calculated exchange interaction energies $\Delta E = E_{\mathrm{F}} - E_{\mathrm{AF}}$ in the FPA (FPA1 and FPA2) and in a fully self-consistent calculation (full scf). Analogously to the previous discussion for the layers, also in the impurity case the interaction is calculated from the single-particle energies using Lloyd's formula [see Eq. (15)], with the atomic t matrix of the impurities as determined in a self-consistent calculation for a single Co impurity. In FPA1 this t matrix is calculated in the single-site approximation, by neglecting perturbations of the neighboring Cu atoms. In contrast to this in the FPA2 the Co t matrix is determined by allowing also potential and density perturbations of these Cu atoms which is analogous to the procedure used in the IXC calculations. The ''full scf'' data refer to fully self-consistent calculations for the two interacting impurities including charge and magnetization disturbances of the neighboring Cu atoms. Self-consistent calculations have been performed for both the ferromagnetic and the antiferromagnetic configurations and the resulting total-energy difference $E_{\mathrm{F}} - E_{\mathrm{AF}}$ is evaluated, including all double-counting contributions. As one can see the FPA2 values agree very well with the self-consistent results, and also the FPA1 values give the correct trend, e.g., a strong ferromagnetic interaction for nearest neighbor pairs and a weak antiferromagnetic interaction for second neighbors. The improvements of the FPA2 values as compared to FPA1 are due to the improved description of the impurity potential, allowing for charge and magnetization disturbances of the neighboring atoms. Thus we have demonstrated that, in agreement with Oswald *et al.*,[18] the exchange coupling can be reliably calculated from the single-particle energies only.

G. Reason for using finite temperatures

It is known that a strong gain in numerical effort can be made by transforming the energy integral in, e.g., Eq. (27) into a contour integral in the complex plane,[12,22,23] which for zero temperature would look like

$$\int^{\varepsilon_F} g(\varepsilon) d\varepsilon = \oint g(z) dz - \int_C g(z) dz = - \int_C g(z) dz, \tag{29}$$

where $g(z)$ is an arbitrary function (for instance the Green's function) which is analytic on the physical sheet of complex energies z. The closed-loop integral disappears due to the

analyticity of the integrand within its boundaries. In our Green's function calculations the contour C starts at the real energy axis below the minimum of the valence band, goes out in the complex plane, and returns to the real axis at the Fermi energy ε_F. The gain arises from the fact that for real energies the Green's function $G(z)=(z-H)^{-1}$ is strongly structured due to poles and branch points. This structure becomes quickly smoother when leaving the real axis. But since for zero temperature the contour C returns to the real axis at ε_F, the same problem still exists at this energy. While typically the integral along the real axis requires for an accurate evaluation about 1000 energy points, only about 30–50 energy points, of which about one-half have to be placed close to ε_F, are sufficient for the complex contour C.

On the other hand for finite temperatures the integrand has poles in the complex plane, the so-called Matsubara poles of the Fermi-Dirac function at $z_p=\mu+(2p\pm1)\pi ikT$, $p\in\{1,2,\dots\}$, where μ is the chemical potential,

$$\int^{\infty} g(\varepsilon)f(\varepsilon)d\varepsilon = \oint g(z)f(z)dz - \int_{C'} g(z)f(z)dz$$
$$= 2\pi i\sum_p \mathrm{Res}\, g(z_p) - \int_{C'} g(z)f(z)dz. \tag{30}$$

Now the closed loop contains a fixed number of Matsubara poles and the contour C' returns to the real axis only at infinity. The most effort is connected with the calculation of the residues at the poles z_p. While these approach the real axis for $T\to0$, for finite T the pole closest to the real axis is located at $\mu+i\pi kT$. Thus a finite temperature gives the possibility of introducing a smearing of the structured integrand in a very controlled way, since it never has to be evaluated for real energies. The most important advantage is, however, that the $\mathbf{k}_\parallel$ integration converges for complex energies rather fast, so that only a moderate number of $\mathbf{k}_\parallel$ points is needed.

H. Numerical details

Three different integrations have to be performed for the calculation of the IXC energy, the $\mathbf{k}_\perp$ integration (10) to obtain the Green's function in the planar representation and the $\mathbf{k}_\parallel$ and the complex energy integration for the interaction energies, Eq. (27).

For carrying out the $\mathbf{k}_\perp$ integration in Eq. (10) an extended trapezoidal integration method with about 300 mesh points in the interval $[-\pi/d,+\pi/d]$ was used.

Before the complex energy integration in Eq. (27) is performed, a $\mathbf{k}_\parallel$ integration is carried out for each energy point in the complex plane. As previously mentioned the Green's function $G^0_{iL,i'L'}$ and, with it, the integrand in Eq. (10) become smoother with larger distance from the real axis. Only at the chemical potential μ does the integrand approach the real axis in steps of $2\pi kT$ from one Matsubara pole to the next. For the poles close to the real axis the $\mathbf{k}_\parallel$ integral in Eq. (27) must be carried out with high accuracy because of the stronger structure of the Green's function at these points. For this reason we have adjusted the $\mathbf{k}_\parallel$ mesh to the location of the energy points in the complex plane. For the two Matsubara poles closest to the real axis, at the complex energies $z=\mu+i\pi kT$ and $z=\mu+i3\pi kT$, respectively, and for a temperature of $T=473$ K, we use a special-point method[24–26] and take 465 $\mathbf{k}_\parallel$ points in the irreducible wedge of the 2D zone. For the next poles 120 $\mathbf{k}_\parallel$ points turn out to be sufficient. Five poles have been used in total. The other energy points, being located along the complex contour, can be calculated with 45 $\mathbf{k}_\parallel$ points.

Another reason for taking so many $\mathbf{k}_\parallel$ points at the last two Matsubara poles is the oscillatory behavior of the Green's function $G^0_{iL,i'L'}$, varying very rapidly in energy and $\mathbf{k}_\parallel$ space for large layer separations. Since only areas around the stationary points on the Fermi surface determine the behavior of the IXC for large spacer thicknesses, these areas have to be well resolved in the $\mathbf{k}_\parallel$ integration, with a mesh being capable of giving the correct curvature of the Fermi surface at these points; otherwise, it is not possible to get the right asymptotic behavior of the IXC energy.

The fact that mainly the electronic states at the Fermi surface are important for the IXC shows up in the individual contributions of the different energy points. Actually for large spacer thicknesses and a temperature of $T=473$ K the two poles closest to the chemical potential μ give the major contribution.

III. CALCULATIONS FOR Co/Cu/Co(100)

In this section we present the results for the interlayer coupling of (100) Co layers in Cu. For several reasons this system is a very suitable model system. First, Cu is one of the simplest possible spacer materials due to its relatively simple Fermi surface and the fact that no large Stoner enhancement effects are expected within the spacer layer. Second, the magnetic properties of cobalt are rather insensitive to the thickness of the cobalt layer since the majority spin states are filled and the local magnetic moments are more or less saturated. For instance a single monolayer (ML) of Co embedded into Cu has a moment of $1.54\mu_B$, whereas the moments for a Co layer of 3 ML are $1.55\mu_B$, $1.57\mu_B$, and $1.55\mu_B$. Also thicker Co layers have only slightly different moments. A Co layer with the thickness of 7 ML, e.g., has the moments $1.54\mu_B$, $1.58\mu_B$, $1.61\mu_B$, $1.60\mu_B$, $1.61\mu_B$, $1.58\mu_B$, and $1.54\mu_B$. Third, the structural misfits are known to be small between fcc Co and fcc Cu, and last, fcc Co/Cu/Co is one of the experimentally best studied systems which makes a quantitative comparison with experimental data possible.

The system which we present consists of two Co layers perfectly embedded in a Cu host and separated by a variable number of Cu monolayers (up to 32). The thickness of the Co layers is varied from 1 to 11 monolayers. The misfit of the Co atoms and the resulting small tetragonal distortion of these layers are neglected.

A. Results and discussion

As a typical example of our results, Fig. 2 shows the calculated IXC energy as a function of the Cu spacer thickness for three different thicknesses of the Co layers, i.e., 1 ML Co (dashed line), 5 ML Co (dotted line), and 7 ML Co (solid line). The definition of the IXC energy as the differ-

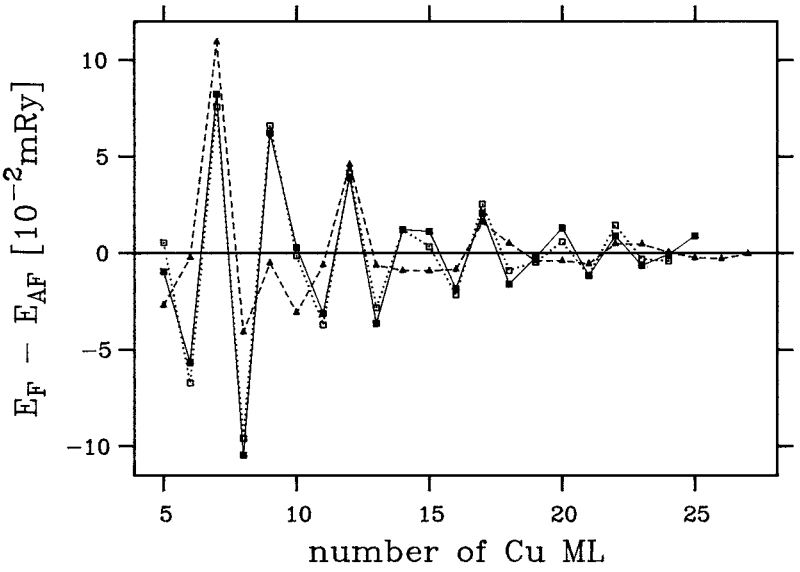

FIG. 2. Calculated exchange coupling (IXC) energies for Co/Cu (100) as a function of the Cu spacer thickness for three different thicknesses of the Co layers, i.e., 1 ML Co (dashed line with triangles), 5 ML Co (dotted line with open squares), and 7 ML Co (solid line with solid squares).

ence $E_F - E_{AF}$ between the ferromagnetic and the antiferromagnetic coupling energies means that for positive IXC values antiferromagnetic coupling is preferred while for negative values the ferromagnetic alignment is stable.

As can be seen from Fig. 2 the results for 5 and 7 ML Co are very similar, but differ strongly from the results for 1 ML. In fact our calculations show that for Co thicknesses larger than 3 ML always very similar results are obtained, so that only the values for 1 and 2 ML Co are exceptional. For 1 ML Co, Fig. 2 shows antiferromagnetic maxima at 7, 12, 17, and 22 ML Cu. In contrast to this the results for 5 and 7 ML Co show additional antiferromagnetic peaks at 9, 14–15, and 20 ML Cu. In addition we also obtain two strong antiferromagnetic peaks at shorter distances (2 and 4 ML) which are not presented in Fig. 2. Due to pinhole effects, antiferromagnetic peaks usually cannot be observed at shorter distances.

These results for the IXC as a function of the spacer thickness will be discussed and explained in detail in the following subsections. Here we will concentrate on the dependence on magnetic layer thickness which can also be shown in a different way. In Fig. 3 the coupling strength is given as a function of the Co layer thickness for fixed spacer thicknesses of 7, 9, 12, and 15 ML Cu, corresponding to the first antiferromagnetic peaks in Fig. 2. As can be seen the coupling varies strongly from 1 to 3 ML Co, but for larger Co thicknesses only small oscillations around a stationary asymptotic value are found. This result is in accordance with predictions of Bruno[10] and a free electron model study of Barnaś.[11] In the experimental work of Qiu *et al.*[27] no dependence of the IXC on the Co thickness is found for thicknesses larger than 8 ML Co. Recently Bloemen *et al.*[28] have carried out measurements for smaller thicknesses, where they find a fastly decreasing coupling strength with decreasing number of Co ML. For larger Co thicknesses up to 10 ML they observe a similar oscillatory behavior as found here, with a period of 3.3 ML. Thus the experimental results are in good agreement with our calculations, even if, as our calculations show, the behavior for 1 and 2 Co ML is more complicated. It should be noted that due to roughness the inter-

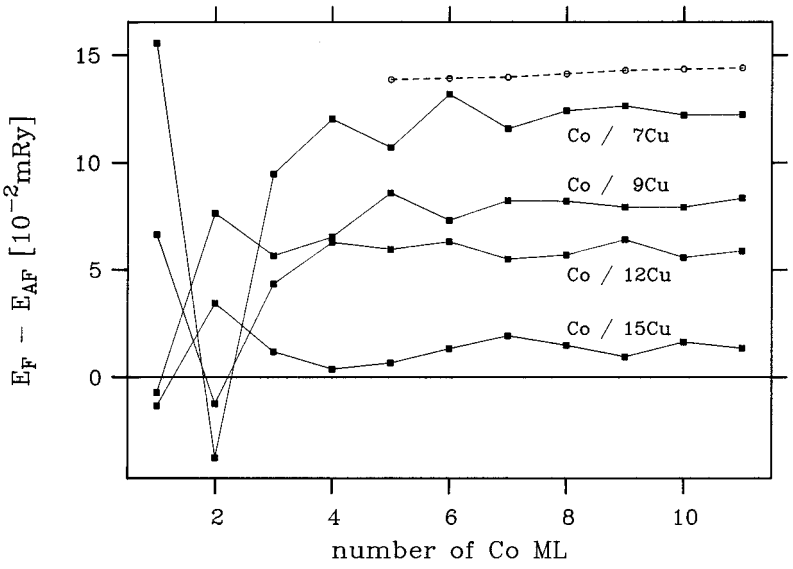

FIG. 3. Exchange coupling energies of Co/Cu(100) as a function of the number of Co layers for Cu thicknesses of 7, 9, 12, and 15 ML.

pretation of the experimental results seems to be more complicated than initially assumed.[29] A detailed comparison of our results with experiments is postponed to Sec. III D, since a meaningful comparison requires the discussion of roughness effects.

B. Asymptotic analysis

The RKKY formulation of the IXC (Refs. 3,4) is, as mentioned above, only valid for large interlayer distances. Within this model, being equivalent to the second-order expression (28), the IXC energy is expressed by the superposition of several independent oscillations stemming from extremal spanning vectors, so-called calipers, of the Fermi surface of the spacer material,

$$E_{\mathrm{RKKY}}=\sum_i A_i \sin(2\pi z/\lambda_i+\phi_i)/z^2. \tag{31}$$

Thus the contribution of each caliper is characterized by three parameters, the wavelength λ_i, the amplitude A_i, and the phase shift ϕ_i. For Cu in the (100) orientation there are two different oscillation periods corresponding to the shorter and longer vertical calipers of the ''dogbone'' of the Cu Fermi surface. Therefore, for large Cu interlayer thicknesses our results in (100) orientation should be representable as a superposition of these two oscillations. In order to understand the drastic changes in the interlayer coupling when going from 1 ML Co to thicker magnetic layers of 3 ML and more we have performed least squares fits of our calculated data to the RKKY expression of Eq. (31). As a representative for thick magnetic layers, we take the result for 5 ML Co. The fitting parameters are the wavelengths λ_S and λ_L and the corresponding amplitudes (A_S, A_L) and phases (ϕ_S, ϕ_L) of the short and long periods, respectively. We fit our calculated data between 8 and 22 ML Cu and find that both curves are actually superpositions of the same two oscillations with wavelengths $\lambda_S=2.60\pm0.02$ ML and $\lambda_L=5.9\pm0.4$ ML, respectively. These two oscillation periods correspond closely to values estimated from de Haas–van Alphen data.[3] The crucial difference between a thin and thick Co layer is the relative magnitude of the amplitudes of the two oscillations, A_S and A_L. For 1 ML Co the amplitudes are about of the same order, $A_S/A_L=0.74$, with the amplitude of the 6 ML wavelength oscillation being somewhat larger, but for 5 ML Co the short-wavelength oscillation totally dominates, $A_S/A_L\cong10$. [These numbers depend somewhat on the details of the fits, like the number of Cu layers taken into account and the estimated starting values of the fitting parameter. In addition the calculated results, based on the exact expression (27) instead of (28), include also contributions from higher harmonics of the wavelengths λ_i, which cannot be represented by Eq. (31). The ratio $A_S/A_L=17$ given in Ref. 9 resulted from a less accurate fit over a too large Cu interval.] Thus by changing the Co thickness from 1 ML to thicker layers, we observe a dramatic redistribution of weight between the two oscillation periods, such that for larger Co thicknesses the long period is strongly suppressed.

As already discussed in Refs. 7 and 9, a good fit to the calculated data is only obtained for spacer distances larger than 8–10 ML Cu. Thus the asymptotic analysis is restricted to rather large distances. Nevertheless, also for shorter distances the calculated results show a qualitative similarity to the asymptotic behavior.

In Ref. 9 we have analyzed the different oscillations in the IXC energy by dividing the $\mathbf{k}_\parallel$ integration over the 2D BZ in Eq. (27) into a sum of integrals over nonoverlapping areas centered around a stationary point as shown in Fig. 1. For Cu there exist five stationary points within the 2D BZ, with the two inequivalent ones situated at $\mathbf{q}_1=0=\bar{\Gamma}$ and $\mathbf{q}_2=(1.08,0)\pi/a$ where a is the lattice constant. They correspond to the calipers giving rise to the long- ($\mathbf{q}_1$) and short- ($\mathbf{q}_2$) period oscillations, respectively.

As discussed in Ref. 9 the $\mathbf{q}_2$ contribution is strikingly insensitive to Co layer thickness. This can also be seen in Fig. 3. There the open circles connected by the dashed line represent the $E(\mathbf{q}_2)$ contribution as a function of the number of magnetic monolayers for a Cu interlayer thickness at 7 ML (first antiferromagnetic peak in Fig. 2). They clearly show no oscillatory behavior. Or, to formulate it in another way, the oscillations in the IXC energy E_{IXC} in Fig. 3 for large magnetic layer thicknesses are caused by the $\mathbf{q}_1$ contribution alone.

C. Interaction with Co *d* states

As we have seen in the last two sections, the two independent IXC contributions $E(\mathbf{q}_1)$ and $E(\mathbf{q}_2)$ show a very different dependence on the magnetic layer thickness. In particular for thicker Co layers the short-wavelength contribution $E(\mathbf{q}_2)$ clearly dominates. This $\mathbf{k}_\parallel$ dependence of the coupling should be caused by the local electronic structure of the embedded Co layer and its interaction with those Cu states relevant for the IXC.

Due to the nearly saturated spin moment of Co, the Co potential for the majority spin states is very close to the Cu potential, whereas the Co minority potential is more repulsive. Therefore the Bloch states of Cu scatter strongly at the minority potential, but only weakly at the majority one. As a consequence of this, for an antiferromagnetic coupling of the Co layers, the Cu Bloch states scatter for each spin direction always weakly at one of the two interfaces, so that the IXC is expected to be weak for the antiferromagnetic configuration. In contrast to this, for a ferromagnetic alignment a strong scattering is expected in the minority spin channel at both interfaces, so that a strong contribution to the IXC is expected. This is confirmed by the calculations. Figure 4 shows the two individual contributions E_{F} and E_{AF} to the interlayer exchange coupling $E_{\mathrm{IXC}}=E_{\mathrm{F}}-E_{\mathrm{AF}}$ for the ferromagnetic (E_{F}) and antiferromagnetic alignment (E_{AF}) with a Co thickness of 3 ML. The antiferromagnetic coupling contribution is clearly much smaller than the ferromagnetic one. One can also show that the interaction in the ferromagnetic configuration is dominated by the minority spin states which are strongly scattered at both Co layers.

Thus when studying the importance of the electronic structure of the (100) Co layers for the interlayer coupling, one can concentrate on the minority (spin down) states. In addition one knows from the asymptotic RKKY theory[3] that for large spacer thicknesses only states with $\mathbf{q}_\parallel$ values close to the stationary points $\mathbf{q}_1$ and $\mathbf{q}_2$ and with energies close to ε_F can affect the interlayer coupling.

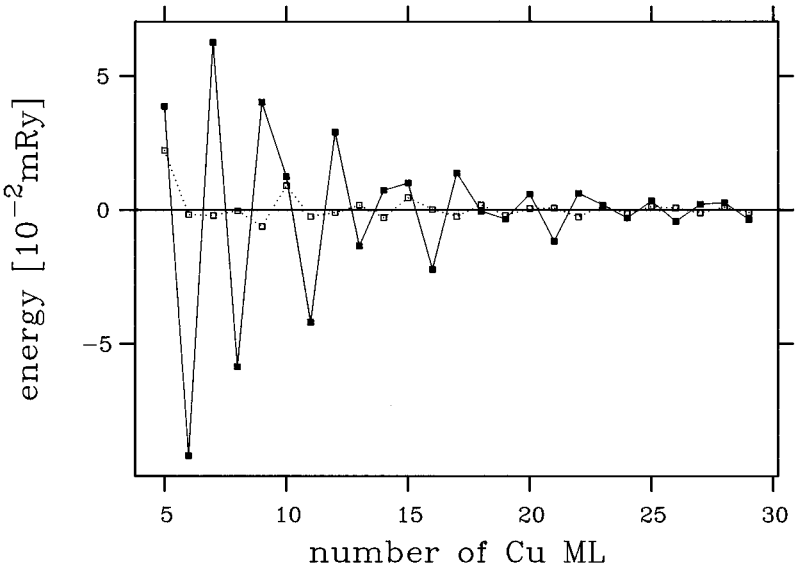

FIG. 4. The individual contributions E_{F} and E_{AF} to the interlayer exchange coupling $E_{\mathrm{IXC}}=E_{\mathrm{F}}-E_{\mathrm{AF}}$ for the ferromagnetic (E_{F}, solid line) and antiferromagnetic (E_{AF}, dotted line) configurations as a function of the spacer thickness. The thickness of the Co layer is 3 ML.

Finally a further selection rule exists arising from the symmetry of the Cu states at ε_F. Figure 5 shows the band structure $E_\nu(\mathbf{k}_\parallel,k_z)$ of Cu as a function of k_z for the two stationary $\mathbf{k}_\parallel$ values $\mathbf{q}_1$ [Fig. 5(a)] and $\mathbf{q}_2$ [Fig. 5(b)]. For the $\mathbf{q}_1=0$ case the Cu states at ε_F are Δ_1 states with a strong p_z contribution. The Δ_1 states are invariant under all cubic symmetry operations which transform the z axis into itself. In the Co layers, only states with the same Δ_1 symmetry can couple to these Cu electrons. Analogously for the $\mathbf{q}_2$ point the Cu states with $\mathbf{k}=(\mathbf{q}_2,k_z)$ near ε_F (solid line) are invariant under a specular reflection at the x-z plane and can therefore only couple to Co states having this symmetry. Summarizing, only minority Co states with energies at ε_F, $\mathbf{k}_\parallel$ equal to $\mathbf{q}_1$ or $\mathbf{q}_2$, and with the same symmetry as the relevant Cu states can affect the interlayer coupling for large distances.

It is therefore important to look at the number of states available in the Co layer which satisfy these selection rules. When no such states exist at all, then a Cu Bloch wave cannot enter into the Co layer and is totally reflected at the interface. In this case the IXC should be optimally strong. On the other hand, if many Co states satisfy the selection rule, then a Cu Bloch wave can propagate into the Co layer, so that the interaction is strongly reduced. Figure 6(a) shows the relevant partial DOS $\Delta n(\mathbf{k}_\parallel,\varepsilon)$ for $\mathbf{k}_\parallel=0$ and projected to Δ_1 symmetry as a function of the energy and for various Co thicknesses. Here Δn refers to the changes of the minority DOS induced by a single Co layer in bulk Cu and is obtained by differentiating the corresponding partial IDOS given by Lloyd's formula [Eq. (13)]. For 1 ML Co we obtain a single resonance, a ''virtual bound state,'' arising from a d_{z^2} state being centered below the Fermi energy.

For n ML Co the n d_{z^2} states interact and form n hybrides ranging from bonding to antibonding states. For large Co thicknesses the part of the DOS shown in Fig. 6(a) represents the highest-lying antibonding states. This explains the fact that the $E(\mathbf{q}_1)$ contribution is reduced for thicker Co layers, as was shown in Fig. 4: The Cu Bloch states at the Fermi energy can propagate through the Co layer via the d states of

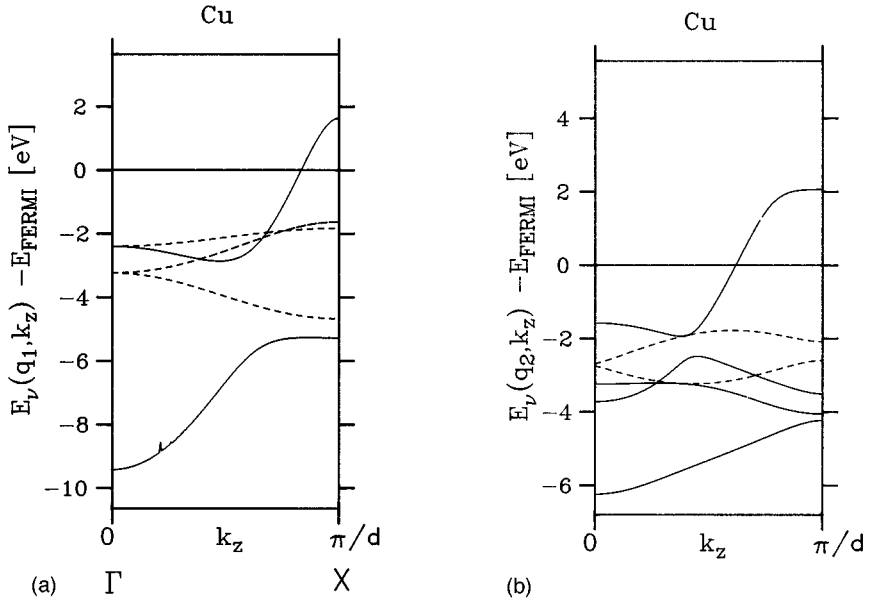

FIG. 5. Band structure $E_\nu(\mathbf{k}_\parallel,k_z)$ of Cu as a function of k_z for the two stationary $\mathbf{k}_\parallel$ values $\mathbf{q}_1=0$ (a) and $\mathbf{q}_2=(1.08,0)\pi/a$ (b). The solid line in (a) refers to states with Δ_1 symmetry, in (b) to states being invariant to a specular reflection at the x-z plane. In both cases these are the states prevailing at the Fermi energy.

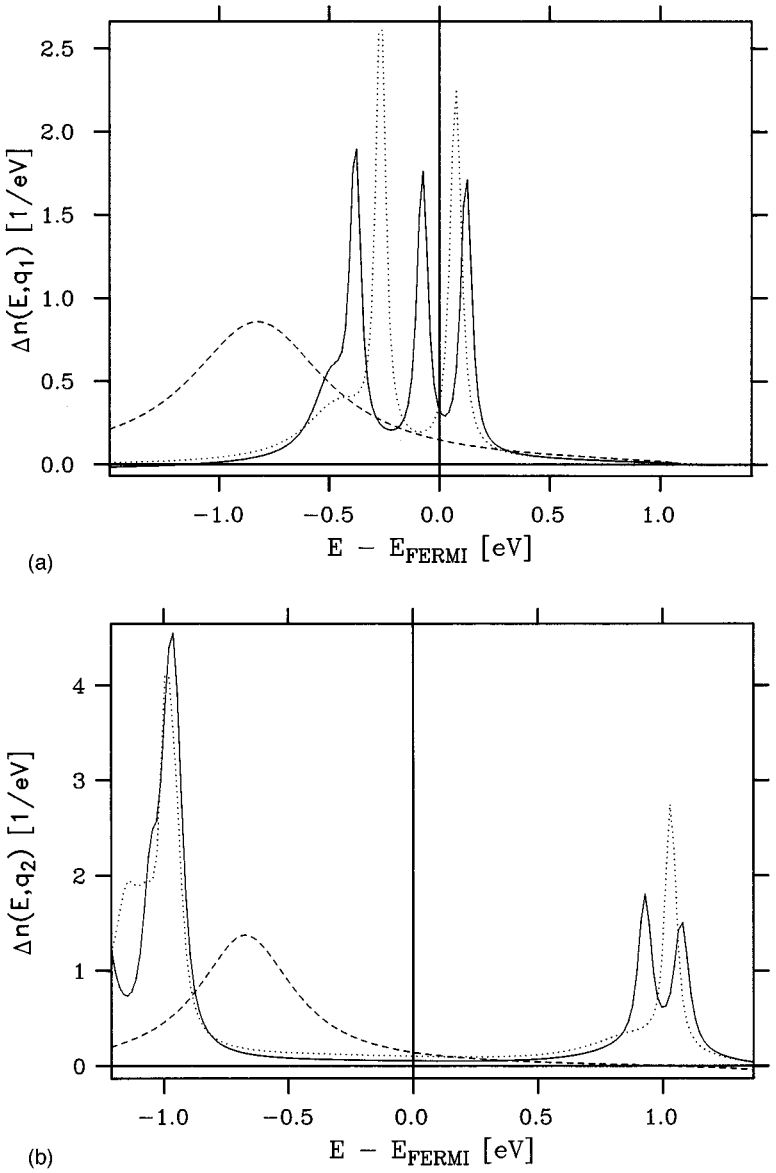

FIG. 6. Partial and $\mathbf{k}_\parallel$ projected density $\Delta n(\mathbf{k}_\parallel, E)$ for minority electrons in the Co layer for the stationary $\mathbf{k}_\parallel$ values $\mathbf{q}_1 = 0$ (a) and $\mathbf{q}_2$ (b). The dashed line refers to 1 ML Co, the dotted one to 5 ML, and the solid line to 7 ML Co. In (a) only states with Δ_1 symmetry are given, in (b) only states with specular reflection symmetry at the x-z plane.

Co. The oscillation of the IXC with respect to the magnetic layer thickness was explained by Bruno[10] as due to interference of Bloch states scattering at the front and the back interfaces of the Co layer. Another, complementary, picture is that the Cu states scatter at the size-quantized d states in the Co layer. Since the energy position of these states varies with the Co thickness, this effect gives rise to a magnetic layer dependence in the $E(\mathbf{q}_1)$ coupling. For thick Co layers these d states evolve into the Δ_1 band close to the Γ point which is shown in Fig. 7(a) below. However, even for rather large thicknesses the individual resonances are well resolved and do not overlap. The above discussion is slightly different from Bruno's arguments that the magnetic layer thickness oscillations should arise from the ε_F crossing closest to the X point, i.e., the more sp-like part of the band.

Figure 6(b) shows the corresponding partial DOS $\Delta n(\mathbf{q}_2, \varepsilon)$ with proper symmetry for the $\mathbf{q}_2$ point. For 1 ML Co we observe a similar behavior as for the stationary point $\mathbf{q}_1$, i.e., a single virtual bound state below ε_F. However, for larger Co thicknesses the higher-lying states either center well above or below the Fermi energy, thus effectively opening a gap at the Fermi energy. This is indeed what happens for thicker Co layers resembling the behavior of bulk Co. Figures 7(a) and 7(b) show the band structures $E_\nu(\mathbf{k}_\parallel, k_z)$ for minority electrons of bulk fcc Co as a function of k_z by fixing the $\mathbf{k}_\parallel$ value to $\mathbf{q}_1$ [Fig. 7(a)] and $\mathbf{q}_2$ [Fig. 7(b)]. Whereas for $\mathbf{q}_1$ one obtains a band of "allowed" Δ_1 symmetry (solid lines) at E_F, for the $\mathbf{q}_2$ point only states of "forbidden" symmetry (dashed lines) exist at ε_F, which cannot couple to the relevant Cu states. Thus the partial DOS of allowed states has indeed a gap at ε_F which explains the behavior of the IXC contribution $E(\mathbf{q}_2)$ discussed in Ref. 9. Compared to 1 ML Co, the interaction energy $E(\mathbf{q}_2)$ increases since a gap opens up in the Co layer. Since this gap is rather large, already for moderate Co thickness the Cu Bloch waves can no longer easily penetrate the Co layer and are almost totally reflected, thus explaining the insensitivity of $E(\mathbf{q}_2)$ with respect to the Co thickness.

As we have seen the properly symmetry-projected and $\mathbf{k}_\parallel$-dependent Co DOS can be substantially different for the two stationary points $\mathbf{q}_1$ and $\mathbf{q}_2$ and can change drastically with Co thickness, despite the fact that the overall electronic

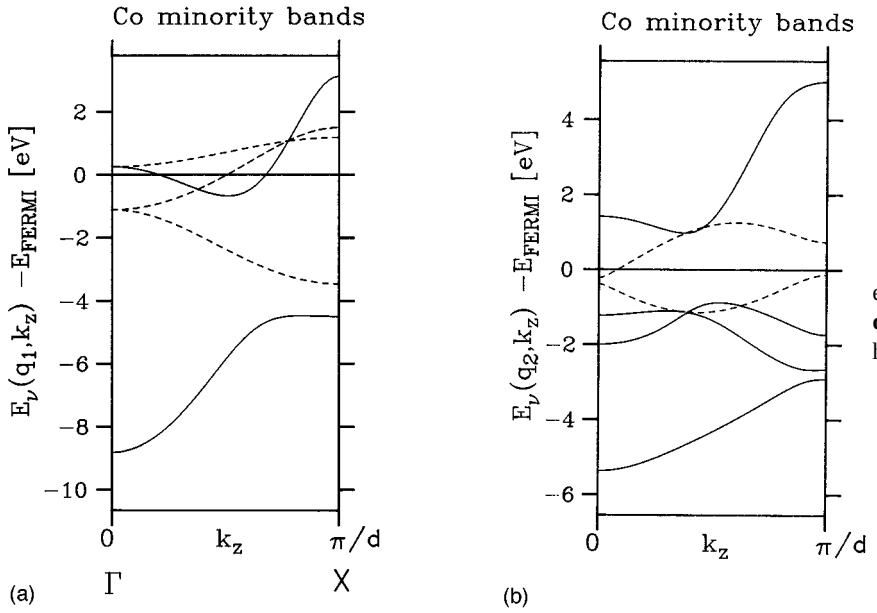

FIG. 7. Band structure $E_\nu(\mathbf{k}_\parallel, k_z)$ of minority electrons in bulk Co as a function of k_z for $\mathbf{q}_1 = 0$ (a) and $\mathbf{q}_2$ (b). The solid and dashed lines have the same meaning as in Figs. 5(a) and 5(b).

structure of the Co layer does not vary appreciably. The formation of bands and gaps at the two stationary points leads to the observed strong redistribution of weights between the two oscillations when the Co thickness is varied.

D. Simulation of interface roughness

It is well known that interface roughness can appreciably affect the IXC. In particular short-period oscillations tend to be suppressed. Here we introduce a model to describe the ''macroscopic'' roughness introduced by steps: We assume that a spacer layer with an average thickness x consists of large patches with n, $n\pm1$, and $n\pm2$ ML thicknesses. Let $P_n(x)$ be the probability to find a spacer thickness of exactly n ML when x is the average (noninteger) thickness. Then the average IXC energy $\bar{E}(x)$ is given by

$$\bar{E}(x) = \sum_n E_n P_n(x), \tag{32}$$

where E_n are the ideal IXC energies for spacers with n ML. The thickness distribution functions $P_n(x)$ have to satisfy the relations

$$\sum_n P_n(x) = 1, \quad \sum_n n P_n(x) = x, \tag{33}$$

where the first one describes the normalization and the second one the definition of the average thickness x.

For the case of ideal growth the function $P_n(x) = P_n^{(0)}(x)$ increases linearly in the interval $n-1 \leqslant x \leqslant n$ from 0 to 1 and then decreases again from 1 to 0 for $n \leqslant x \leqslant n+1$, as shown in Fig. 8. Therefore the IXC function $\bar{E}^{(0)}(x)$ attains the values $E_n, E_{n+1}, \ldots$ at the integer distances $x = n, n+1, \ldots$ while for noninteger distances x neighboring E_n values are linearly interpolated. Thus for ideal growth the $\bar{E}(x)$ function is identical to the curves shown in Fig. 1, consisting of piecewise straight lines connecting neighboring E_n values.

In order to simulate roughness we assume first that the width of the distribution $P_n(x)$ is independent of the thickness, i.e., $P_n(x) = p(z)$, where $z = n - x$ describes the deviation from the average thickness x. This approximation can only be valid in a certain range of thicknesses. We then introduce broadened distribution functions $p^{(i)}(z)$ by a recursion relation

$$p^{(i+1)}(z) = \frac{1}{4}\{p^{(i)}(z-1) + 2p^{(i)}(z) + p^{(i)}(z+1)\}, \quad i \geqslant 0. \tag{34}$$

It is easy to show that this relation preserves the normalization conditions (34). Analogous to the distribution $p^{(0)}(z)$ for ideal growth (shown in Fig. 8), all functions $p^{(i)}(z)$ consist of straight line segments connecting neighboring values $p^{(i)}(z)$ for integer z values. As an example the first three broadened distributions $p^{(1)}(z)$, $p^{(2)}(z)$, and $p^{(3)}(z)$ are shown in Fig. 9 together with the ''ideal'' distribution $p^{(0)}(z)$ of Fig. 8. The progressive broadening seen in Fig. 9 is related to the fact that the variance increases linearly with i,

$$\langle m^2 \rangle \equiv \sum_m m^2 p^{(i)}(m) = \frac{i}{2}, \tag{35}$$

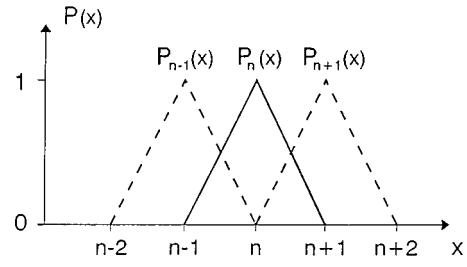

FIG. 8. The thickness distribution functions $P_n(x)$ versus the average thickness x for ideal growth.

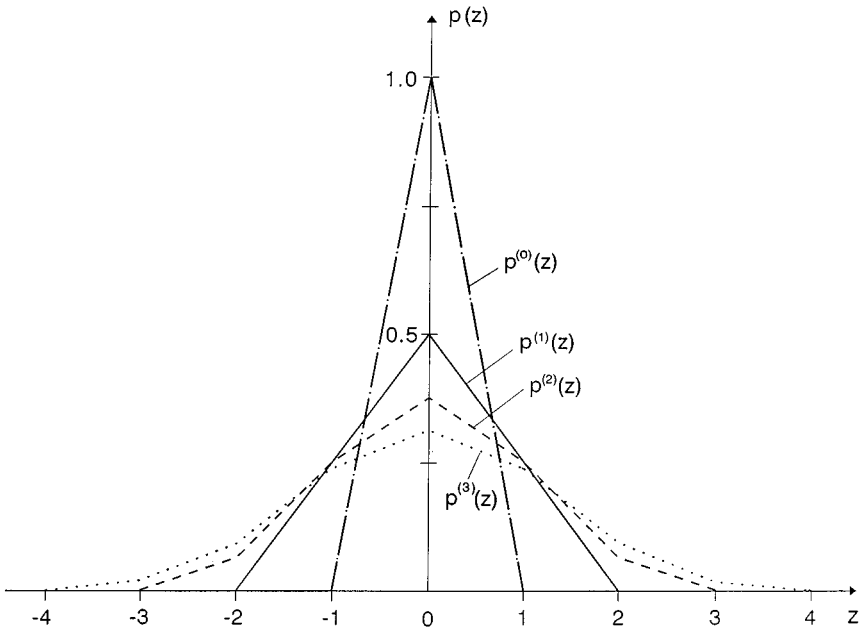

FIG. 9. The model distribution function $p^{(i)}(z)$, $i=1,2,3$, describing the effect of roughness. The variance of $p^{(i)}(z)$, as defined by Eq. (35), is equal to $i/2$.

which follows from Eq. (34). The solution of (34) can also be written in a closed form,

$$p^{(i)}(m)=\frac{1}{2^{2i}}\frac{(2i)!}{(i-m)!(i+m)!}, \tag{36}$$

and approaches a Gaussian for large i. Given these broadening functions $p^{(i)}(m)$ we can calculate the average IXC energies $\bar{E}^{(i)}(x)$. Since these also show a straight line behavior, only the values for the integer x have to be evaluated. The first averages are

$$\bar{E}^{(1)}(n)=\frac{1}{4}(E_{n-1}+2E_n+E_{n+1}),$$

$$\bar{E}^{(2)}(n)=\frac{1}{16}(E_{n-2}+4E_{n-1}+6E_n+4E_{n+1}+E_{n+2}), \tag{37}$$

$$\bar{E}^{(3)}(n)=\frac{1}{64}(E_{n-3}+6E_{n-2}+15E_{n-1}+20E_n+15E_{n+1}+6E_{n+2}+E_{n+3}),$$

and correspond to the broadened distribution functions shown in Fig. 9 which according to Eq. (35) have variances of 1/2, 1, and 3/2, respectively. Scanning tunnel microscope (STM) studies of the surfaces of Co layers deposited on Cu (100) show that these surfaces consist of patches and islands of different heights, with an average roughness of several monolayers. Thus our roughness model should be well suited for this system.

In Fig. 10 therefore we have averaged our results for ideal interfaces, as given in Fig. 2, in the described way assuming a constant Co thickness of 7 ML. Even for $\bar{E}^{(1)}(x)$, corresponding to a modest roughness, the amplitudes of the IXC oscillations are decreased by a factor of 5 and further decreases are seen for $\bar{E}^{(2)}$ and $\bar{E}^{(3)}$. However, equally impor-

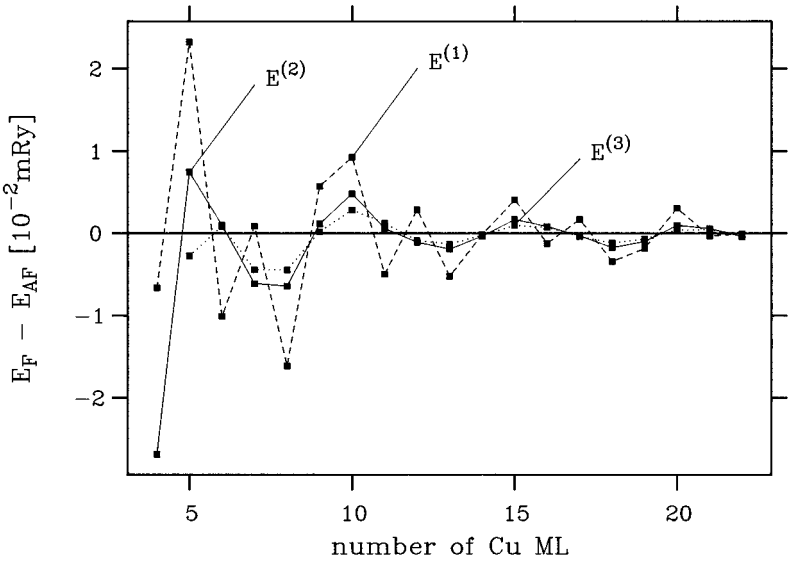

FIG. 10. The average IXC energies $\bar{E}^{(1)}(x)$ and $\bar{E}^{(2)}(x)$ and $\bar{E}^{(3)}(x)$, averaged with the distribution functions $p^{(i)}(z)$ of Fig. 9 to describe the effect of steplike roughness, as a function of the average spacer thickness x. These results for Co/Cu (100) have to be compared with the values of Fig. 2 calculated for ideal interfaces.

TABLE II. Comparison of the calculated and experimentally determined exchange coupling constants J for Co/Cu(100) for the first and second strong antiferromagnetic peaks (in mJ/m^2). The values in brackets give the exact peak positions in Cu ML. $J^{(0)}$ results from the calculated values shown in Fig. 2 for a Co thickness of 7 ML Co and is given by $J=\frac{1}{2}(E_F-E_{AF})/A_{2D}$, where A_{2D} is the unit surface area. $J^{(1)}$ and $J^{(2)}$ are the values obtained for the roughness distributions $p^{(1)}$ and $p^{(2)}$, respectively as shown in Fig. 10.

	$J^{(0)}$	$J^{(1)}$	$J^{(2)}$	Ref. 30	Ref. 31	Ref. 28	Ref. 27
Peak 1	1.42 (7)	0.39 (5)	0.13 (5)	0.40 (6.6)	0.39 (5.2)	0.24 (5.2)	0.16 (6)
Peak 2	0.68 (12)	0.16 (10)	0.08 (10)	0.14 (12)	0.15 (10.3)	0.09 (10.3)	0.06 (11.8)

tant is the fact that the amplitudes of the short period are more strongly reduced than the ones of the long period. While the energy curve $\bar{E}^{(1)}(x)$ still shows weak peaks at 7, 12, and 17 ML, resembling the short-wavelength oscillation, the further broadened curves $\bar{E}^{(2)}(x)$ and $\bar{E}^{(3)}(x)$ are totally dominated by the long period. In contrast to these broadened curves the behavior of ideal interfaces (Fig. 2) is dominated by the short period. Thus depending on the degree of roughness, we observe, together with a reduction of the amplitudes, a crossover from short-period to long-period oscillations. In line with this is a shift of the peak positions to 5, 10, 15, and 20 ML, representing the maxima of the $E(\mathbf{q}_1)$ contribution.

The present roughness simulations fit very well to experimental observations. Johnson *et al.*[30] find strong antiferromagnetic peaks at 6.6 ML, 12 ML, and 17.3 ML, and additional, but somewhat weaker, peaks at about 14.5 and 17 ML. From a RKKY fit to the measured data they estimate the relative amplitude of the short period to long period as 1.25, much smaller than in our calculations for the ideal interface. They do not find the (weaker) antiferromagnetic peak at about 9 ML. As suggested by the authors, this peak is presumably shifted by pinhole effects into the ferromagnetic region. Note that for the same reason no antiferromagnetic peaks are observed for smaller distances, while our calculations yield additional peaks at 2 and 4 ML which are not shown in Fig. 2.

Qiu *et al.*[27] only find the strong antiferromagnetic peaks at about 6, 11.5, and 17 ML. Thus the roughness of their sample seems to be larger than the one of Johnson *et al.*,[30] since the short period is totally suppressed, in the same way as our results are changed with the introduction of the distributions $p^{(2)}$ and $p^{(3)}$ in Fig. 10.

Using an improved technique with three magnetic layers Bloemen *et al.*[31] were able to study also the interaction in the region of ferromagnetic coupling. They indeed find the ''missing'' antiferromagnetic peak as a strong dip in the ferromagnetic coupling curve. Recently Bloemen *et al.*[28] have presented IXC data in connection with their observation of oscillations arising from magnetic layer thickness. The data in Fig. 1 of their paper resemble very well our broadened $E^{(1)}(x)$ curve shown in Fig. 10, as far as both the strength of the additional weak antiferromagnetic peaks as well as the positions of all peaks are concerned. The shift of the whole curve by 2 ML to smaller distances as compared to Johnson *et al.*[30] they attribute to experimental problems. Since we observe the same shift between our unbroadened results in Fig. 2 and the broadened $\bar{E}^{(1)}(x)$ curve in Fig. 10, it seems to be likely that this effect is a consequence of the somewhat larger roughness in the samples of Bloemen *et al.*[28]

A quantitative comparison of the measured and calculated IXC values is made in Table II. Listed are the amplitudes of the first and second strong antiferromagnetic peaks (in mJ/m^2), with the values in the brackets denoting the peak position. Three ''theoretical'' results are given, the calculated ones $E^{(0)}(n)$ of Fig. 2 and the averaged values $\bar{E}^{(1)}(n)$ and $\bar{E}^{(2)}(n)$ of Fig. 10 for the thickness distributions $p^{(1)}(x)$ and $p^{(2)}(x)$ of Fig. 9. Thus while the calculated values are much larger than the experimental results, the data $\bar{E}^{(1)}$ corrected for roughness with the distribution $p^{(1)}(x)$ are in good agreement with the data of Refs. 28, 30, and 31 for intermediately rough interfaces, while the $\bar{E}^{(2)}$ values for the broader distribution $p^{(2)}(x)$ agree well with the data of Ref. 27 for rougher interfaces.

In conclusion our simple simulations give a remarkably consistent picture of the large effects of roughness on IXC in Co/Cu(100). They explain the strong reduction of the amplitudes, the suppression of the short period, and the shift of the peak positions, all effects being observed experimentally.

After the paper was finished we obtained two preprints relevant to this work. Mathon *et al.*[32] calculated the exchange coupling of two semi-infinite Co crystals separated by Cu layers in (100) orientation. While qualitatively their results are similar to ours, in detail important differences exist. The calculated exchange interaction for the first antiferromagnetic peak is about a factor 2 (or 4, if the asymptotic expression is used) smaller than our value for thicker Co layers. Moreover the authors obtain an extremely large amplitude ratio A_S/A_L of about 100–200 (Refs. 32,33) so that practically no long-period contribution exists. While Mathon *et al.* stress the good agreement of the calculated coupling energies with experimental values, we believe that this agreement is accidental and will disappear when realistic corrections for interface roughness, as discussed in Sec. III D, are applied. The average values $\bar{E}(x)$ are then much too small and in particular contain no long-period contribution.

Using spin-polarized scanning electron microscopy Weber *et al.*[34] studied exchange coupling in Co/Cu (100) as well as in related asymmetrical systems like Fe/Cu/Co and Ni/Cu/Co. In Co/Cu samples of varying quality they observe both long- as well as short-period oscillations. For their ''best'' sample showing a pronounced short period they estimate an amplitude ratio $A_S/A_L>7$. The appearance of the short-period oscillation and the large-amplitude ratio agree well with our calculations and, according to Sec. III D, point to a good quality of the sample.

Lee and Chang[35] presented recently tight-binding (TB) calculations (based on an asymptotic analysis) for the inter-

action of two semi-infinite Co crystals. For Co/Cu(001) these authors obtain an extremely small intensity of the long period, with an amplitude ratio $A_S/A_L \approx 320$, in qualitative agreement with Mathon *et al.*,[32] but in disagreement with our results and with the experiments. Recent calculations by Kudrnovsky *et al.*[36,37] seem to show the reason for this discrepancy. While we have only treated Co layers up to thicknesses of 11 Co ML, these authors performed calculations based on the TB linear muffin-tin orbital (LMTO) method for up to 25 Co ML as well as for the case of infinite Co thickness. While in the range of smaller Co thicknesses good qualitative agreement with our results is obtained, i.e., a strong short period and a moderately strong long period, for large Co thicknesses beyond 15–20 Co ML the intensity of the long period seems to decrease appreciably, in qualitative agreement with the above results for the infinite Co thickness. Note that the experiments are performed in the region of small Co thicknesses treated in our calculations.

IV. SUMMARY AND CONCLUSIONS

In summary we have presented calculations for the exchange coupling in Co/Cu (100) by applying a KKR Green's function method for planar perturbations. The use of the frozen potential approximation allows a direct calculation of the interlayer exchange coupling in terms of the single-particle energies, thus avoiding new self-consistent calculations for the interacting system and the subtraction of large total-energy values. In this way efficient calculations can be performed for large distances. In addition the asymptotic behavior of the oscillations can be analyzed by subdividing the 2D Brillouin zone into areas around the different stationary points $\mathbf{q}_i$.

Our results for Co/Cu(100) show that for thick magnetic layers the coupling is dominated by the short wavelength of the RKKY oscillation, whereas for a Co monolayer the longer period is more important. We explain this behavior in terms of the electronic structure of the single Co layer, in particular the $\mathbf{k}_\parallel$-dependent and symmetry-projected DOS of the Co minority electrons. For the stationary point $\mathbf{q}_1 = 0$, determining the longer-period oscillation, a band of Co *d* states evolves with increasing Co thickness at the Fermi energy, enabling the Cu Bloch electrons to propagate through the Co layer and thus reducing the interaction. In contrast to this, for the stationary point $\mathbf{q}_2$, being responsible for the shorter period, a band gap opens up at ε_F for thicker Co layers, thus leading to the dominance of the short-period contribution to the IXC.

In order to compare with experiments we simulate roughness caused by steps by introducing distribution functions for the spacer thickness. The inclusion of roughness in our calculation strongly reduces the interaction in general and especially the short-period oscillation. This is in accordance with experimental work on different samples of varying qualities. For rougher samples[27] only the long period is observed while for the intermediate roughness, present in the samples of the Philips group,[28,30,31] both periods are observed with about the same strength.

In total we obtain good agreement with experiments and a consistent picture of the interlayer exchange coupling in Co/Cu(100).

ACKNOWLEDGMENTS

P.L. thanks the German Academic Exchange Service (DAAD) for financial support, and the Brookhaven National Laboratory and in particular Dr. M. Weinert for their hospitality. L.N. thanks the Swedish Natural Science Research Council for financial support. The calculations were performed on the CRAY computers of the Höchstleistungsrechenzentrum (HLRZ) and the Forschungszentrum Jülich.

*Also at Institute of Computational Science and Informatics, George Mason University, Fairfax, Virginia and Complex System Theory Branch, Naval Research Laboratory, Washington, DC.

[1] P. Grünberg *et al.*, Phys. Rev. Lett. **57**, 2442 (1986).
[2] S. S. P. Parkin, N. More, and K. P. Roche, Phys. Rev. Lett. **64**, 2304 (1990).
[3] P. Bruno and C. Chappert, Phys. Rev. Lett. **67**, 1602 (1991); Phys. Rev. B **46**, 261 (1992); P. Bruno, *ibid.* **52**, 411 (1995).
[4] M. D. Stiles, Phys. Rev. B **48**, 7238 (1993); F. Herman, J. Sticht, and M. Van Schilfgaarde, in *Magnetic Thin Films, Multilayers and Surfaces*, edited by S. S. P. Parkin, MRS Symposia Proceedings No. 231 (Materials Research Society, Pittsburgh, 1991), p. 195; F. Herman, M. Van Schilfgaarde, and J. Sticht, Int. J. Mod. Phys. B **7**, 425 (1993).
[5] F. Herman, J. Sticht, and M. van Schilfgaarde, J. Appl. Phys. **69**, 4783 (1991); M. Van Schilfgaarde *et al.*, Phys. Rev. Lett. **74**, 4063 (1995).
[6] M. van Schilfgaarde and F. Herman, Phys. Rev. Lett. **71**, 1923 (1993).
[7] P. Lang, L. Nordström, R. Zeller, and P. H. Dederichs, Phys. Rev. Lett. **71**, 1927 (1993).
[8] S. Mirbt, H. L. Skriver, M. Aldén, and B. Johansson, Solid State Commun. **88**, 331 (1993).
[9] L. Nordström, P. Lang, R. Zeller, and P. H. Dederichs, Phys. Rev. B **50**, 13 058 (1994).
[10] P. Bruno, Europhys. Lett. **23**, 615 (1993).
[11] J. Barnaś, J. Magn. Magn. Mater. **111**, L215 (1992).
[12] R. Zeller, P. Lang, B. Drittler, and P. H. Dederichs, in *Application of Multiple Scattering Theory to Materials Science*, edited by W. H. Butler, P. H. Dederichs, A. Gonis, and R. Weaver, MRS Symposia Proceedings No. 253 (Materials Research Society, Pittsburgh, 1992), p. 357.
[13] P. J. Braspenning, R. Zeller, A. Lodder, and P. H. Dederichs, Phys. Rev. B **29**, 703 (1984).
[14] P. Lloyd, Proc. Phys. Soc. London **90**, 207 (1967).
[15] A. Oswald, R. Zeller, and P. H. Dederichs, Phys. Rev. Lett. **56**, 1419 (1986).
[16] B. Drittler, M. Weinert, R. Zeller, and P. H. Dederichs, Phys. Rev. B **39**, 930 (1989).
[17] This is also known as the ''force theorem;'' see, e.g., D. G. Pettifor, Commun. Phys. **1**, 141 (1977).
[18] A. Oswald, R. Zeller, P. J. Braspenning, and P. H. Dederichs, J. Phys. F **15**, 193 (1985).
[19] D. Mermin, Phys. Rev. **137**, A1441 (1965).
[20] K. Wildberger, P. Lang, R. Zeller, and P. H. Dederichs, Phys. Rev. B **52**, 11 502 (1995).

[21] F. Gautier, G. Moraitis, and J. C. Parlebas, J. Phys. F **6**, 381 (1976).
[22] R. Zeller, J. Deutz, and P. H. Dederichs, Solid State Commun. **44**, 993 (1982).
[23] C. Koenig, J. Phys. F **3**, 1497 (1973).
[24] H. J. Monkhorst *et al.*, Phys. Rev. B **13**, 5188 (1976).
[25] W. R. Fehlner and S. H. Vosko, Can. J. Phys. **55**, 2041 (1976).
[26] A. H. MacDonald, Phys. Rev. B **18**, 5897 (1978).
[27] Z. Q. Qiu, J. Pearson, and S. D. Bader, Phys. Rev. B **46**, 8659 (1992).
[28] P. J. H. Bloemen *et al.*, Phys. Rev. Lett. **72**, 764 (1994).
[29] P. J. H. Bloemen *et al.* (unpublished).
[30] M. T. Johnson *et al.*, Phys. Rev. Lett. **68**, 2688 (1992).
[31] P. J. H. Bloemen *et al.*, J. Appl. Phys. **73**, 5972 (1993).
[32] J. Mathon *et al.*, Phys. Rev. Lett. **74**, 3696 (1995).
[33] J. Mathon *et al.* (unpublished).
[34] W. Weber, R. Allenspach, and A. Bischof, Europhys. Lett. **31**, 431 (1995).
[35] B. Lee and Y.-Ch. Chang, Phys. Rev. B **52**, 3499 (1995).
[36] J. Kudrnovsky, V. Drchal, I. Turek, and P. Weinberger, Phys. Rev. B **50**, 16 105 (1994).
[37] J. Kudrnovsky, V. Drchal, I. Turek, M. Sob, and P. Weinberger, Phys. Rev. B **53**, 5125 (1996).